*Manuscript_clean
Click here to download Manuscript: Revised Manuscript_clean_A-19-1789_R1.docx Click here to view linked References

Effect of electrochemical charging on the hydrogen embrittlement susceptibility of Alloy 718

X. Lu, [a,*] D. Wang, [a] D. Wan, [a] Z.B. Zhang, [b] N. Kheradmand, [a] A. Barnoush, [a,*]

[a] *Department of Mechanical and Industrial Engineering, Norwegian University of Science and Technology, No-7491 Trondheim, Norway*

[b] *School of Materials, University of Manchester, M13 9PL, UK*

Corresponding author 1: Afrooz Barnoush

Email: afrooz.barnoush@ntnu.no

Postal address: Department of Mechanical and Industrial Engineering (MTP), Norwegian University of Science and Technology (NTNU), Richard Birkelandsvei 2B, NO-7491 Trondheim, Norway

Corresponding author 2: Xu Lu

Email: xu.lu@ntnu.no

Postal address: Department of Mechanical and Industrial Engineering (MTP), Norwegian University of Science and Technology (NTNU), Richard Birkelandsvei 2B, NO-7491 Trondheim, Norway

Abstract

The susceptibility of age-hardened nickel-based 718 superalloy to hydrogen embrittlement was studied by the controlled electrochemical charging combined with slow strain-rate tensile tests (SSRT) and advanced characterization techniques. We proposed some novel ideas of explaining hydrogen embrittlement mechanisms of the studied material in regard to two cracking morphologies: transgranular and intergranular cracking. It is for the first time to report that electrochemical charging alone could cause slip lines, surface and subsurface cracks on nickel-based superalloys. The formation of pre-damages was discussed by calculating the hydrogen concentration gradient generated during cathodic charging. Pre-damages were proved to result in transgranular cracks and lead to the evident reduction of mechanical properties. In addition, the STRONG (Slip Transfer Resistance of

Neighbouring Grains) model was used to analyze the dependence of hydrogen-assisted intergranular cracking on the microscopic incompatibility of the grain boundaries. The results show that in the presence of hydrogen, grain boundaries with a lower dislocation slip transmission are more prone to cracking during loading and vice versa.

Keywords: Hydrogen embrittlement; nickel-based superalloy; hydrogen-induced cracking; electrochemical hydrogen charging; slip transmission.

1 Introduction

Precipitation-hardened nickel-based superalloys, with their combination of excellent mechanical properties, good corrosion resistance, and wide working temperature range, are some of the best candidates used for subsea oil and gas industries. Despite their good mechanical properties, these high-strength alloys are susceptible to hydrogen embrittlement (HE) when they are used in a hydrogen-containing environment [1-9]. The mechanism of HE has been extensively debated for decades [10]. Both experimental techniques and computational models were applied to unravel the hydrogen-assisted failure process [11-13]. Several acceptable mechanisms proposed thus far include hydrogen-enhanced localized plasticity (HELP) [12, 14, 15], hydrogen-enhanced decohesion (HEDE) [7, 16-18], hydrogen adsorption-induced dislocation emission (AIDE) [11, 19-22], hydrogen-enhanced strain-induced vacancy (HESIV) [23] and crack induction by hydride formation [6, 24-26]. Through years of understanding the role of hydrogen in nickel-based superalloys, particularly precipitation-hardened alloys, several prevalent mechanisms were proposed. When this alloy is deformed in hydrogen containing environment, two types of cracking prevail: transgranular and intergranular cracking, which are explained by HELP [3, 27] and HEDE [28, 29] the most. On one hand, recent studies [8, 28, 30] concluded that transgranular cracking originated from the intersections of slip bands. The local stress concentrations and strain discontinuities at the intersection points attract hydrogen, and the local plastic instability in combination with non-uniform hydrogen concentration lead to the primary cracking. On the other hand, hydrogen-assisted intergranular cracking was

observed at delta (δ) phase decorated grain boundaries (GBs) [30], GB triple junctions [28], and high angle GBs [31]. The δ phase was proved to promote GB cracking through forming micro-cracks along its interfaces with the matrix in the framework of HEDE mechanism [7, 28, 29]. In addition, high elastic mismatch and strain localization at GBs and triple junctions facilitate decohesion and crack formation [28]. Kimura and Birnbaum [6] reported that a critical amount of hydrogen is a prerequisite for generating intergranular cracks in nickel alloys depending on the nature of the GBs and the corresponding stress state. Additionally, it has been documented that the cracking behavior of GBs is highly dependent on the misorientation angle [32, 33]. In other words, cracks are likely to initiate at high-angle GBs, while low-angle or low-Σ boundaries are more resistant to fracture [34]. However, to determine whether a GB has a high propensity to cracking or not, the measurement of misorientation alone, which is based on the 2D surface information, is far from being adequate due to the complex structure of GBs and the synergetic effect of adjacent grains upon deformation. During deformation of a polycrystalline metal, some GBs act as barriers for dislocation slip that causes dislocation pile-ups and local stress concentrations [35, 36]. Other GBs allows partial or full transmission of dislocations depending on the deformation behavior of adjacent grains and the character of GBs. By considering this, the concept of slip transferability and its impact on crack initiation along GBs was brought up to analyze the fatigue crack initiation and growth [37, 38]. And 3D characterization of the GB makes it possible to analyze the incompatibility stresses and reveal the transmission of the plasticity across the GB. However, this idea has not been involved in uncovering the underlying mechanisms of materials that failed in the hydrogenating environment. Analyzing stress compatibility of GBs is of great help to understand hydrogen-assisted intergranular cracking behavior.

Moreover, in most of the previous studies, hydrogen was introduced into the material through electrochemical charging. And it is known that harsh charging conditions, especially electrochemical charging, can cause surface damage in the form of blisters on steel and pure iron [39-42]. However, in face-centered-cubic (FCC) metals, where hydrogen diffusion is sluggish, the impact of hydrogen absorption and its influence on the cracking behavior during deformation is rarely documented. The most important reason for

this is the difficulty of preserving a clean surface after long electrochemical hydrogen charging. Thus far, most of the solutions used for electrochemical charging have been water-based, which could cause surface corrosion after charging. In ex-situ tests, further surface polishing before loading would introduce new stresses and thus conceal the useful information of charging. In the case of in-situ tests, what we observe is a combined effect of cathodic charging and mechanical loading, from which it is more difficult to disentangle the HE mechanisms responsible for each type of cracking behavior.

In the present study, a systematic analysis was conducted on the effect of cathodic charging and its subsequent impact on the mechanical properties of age-hardened Alloy 718 superalloys. We used a glycerol-based electrolyte to preserve the surface integrity of the alloy. Thus, direct observations and studies of the influence of electrochemical charging could be realized. The material was cathodically charged and then subjected to direct-surface and subsurface-damage characterization. A linkage between hydrogen-induced pre-cracking and mechanical properties was set up. Later, the 3D information of GBs was collected using Focused ion beam (FIB) cross section milling technique on the failed hydrogenated samples after mechanical loading. We adopted the STRONG (Slip Transfer Resistance of Neighbouring Grains) model proposed by Knorr [43] to analyze the relationship between the slip system compatibility and hydrogen-assisted intergranular cracking behavior. In this manner, we conducted a thorough analysis of the failure behavior of Ni-based superalloys and tried to figure out the factors controlling transgranular and intergranular cracking in the electrochemical charging conditions.

2 Materials and experimental procedure

In this work, the standard UNS N07718 (Alloy 718) alloy was used; its main chemical composition is listed in Table 1. As received from the supplier, the alloy went through standard API heat treatment with an aging temperature of 782 °C for 6.5 h before air cooling. Two-step dog-bone tensile test specimens for the slow strain-rate tensile test (SSRT) were cut by electrical discharge machining (EDM) as shown in Fig. 1(a).

Table 1 Chemical composition of Alloy 718 alloy

Fig. 1 (a) Specimen geometry for slow strain rate tensile test (all dimensions are shown in mm) and (b) schematic of subsurface characterization direction.

Before charging, the specimens were ground sequentially from 220 grit to 4000 grit SiC papers and then polished with 3 μm and 1 μm diamond pastes. Electropolishing was conducted in a methanolic H_2SO_4 solution at 26 V 30 s as the final step to remove the deformed layer by previous mechanical polishing. Ex-situ hydrogen charging was performed in a three-electrode electrochemical charging cell. A platinum net was used as the counter electrode and Ag/AgCl was used as the reference electrode due to its wide working temperature range. The charging process was performed in a 2:1 mixture of glycerol and H_3PO_4 [44, 45] at 75 °C at a constant potential of –1050 mV (equals to a cathodic current density of 15 mA/cm^2). This solution offers the possibility of preserving a corrosion-free surface after electrochemical charging. Later, the specimens were washed with distilled water and ethanol and dried in circulating air flow. The dwell time between finishing hydrogen charging and the damage characterization was controlled within 10 min. In order to study the effect of electrochemical charging, different charging times of 20, 40, 60, 80, 100, 120 and 168 h were chosen.

SSRT was performed at a constant nominal strain rate of 2×10^{-5} s^{-1} on a Kammrath & Weiss tensile/compression module inside the high-resolution Quanta FEG 650 scanning electron microscope (SEM, Thermo Fisher Scientific Inc., USA) for a real-time recording. The specimens were loaded until fracture to study the deformation process and crack evolution in vacuum condition (4.7×10^{-3} Pa) and hydrogen-charged condition. The dwell time before testing was controlled within 30 min. As the diffusion rate of hydrogen in the FCC material is low (about 10^{-15} m^2/s) [46], hydrogen loss within this period was negligible. In order to study the possible damage below the fracture surface, the fractured parts were electrodeposited in a Ni electroplating solution before subsurface analysis to provide appropriate edge retention and mechanical stability during sample preparation. A

dense layer of Ni with about 40 μm thickness was deposited. Afterwards, the coated samples were mounted, grinded and polished. By using a caliper, the sample depth that was removed from the fracture surface was precisely controlled to be 50, 350, and 650 μm perpendicular to the tensile axis, as shown schematically in Fig 1(b). This sectioning process was proved to cause no subsurface damages on the analyzed cross-sections. To study the effect of hydrogen alone, the same subsurface characterization procedure was conducted on the hydrogenated specimens without further mechanical loading. A thorough microstructural characterization on both fracture surfaces and subsurfaces was conducted using SEM embedded with backscattered electron (BSE) and electron dispersive spectroscopy (EDS) detectors. Electron channeling contrast imaging (ECCI) was used to reveal deformation structures after fracture. Electron backscattered diffraction (EBSD) was conducted at an accelerating voltage of 20 kV with a step size of 200 nm-1 μm. Before EBSD characterization, the samples were mechanically polished and finished with a 0.04 μm colloidal silica suspension (OPS) to obtain deformation-free surfaces. FIB (Helios Nanolab DualBeam FIB, Thermo Fisher Inc., USA.) milling was performed to cut a trench across each boundary to achieve a complete grain boundary trace information on orthogonal planes to the sample surface. In addition, thermal desorption spectroscopy (TDS) test was carried out to determine the total hydrogen content in the sample after hydrogen charging. The TDS test was performed by a Bruker G4 PHONIX DH analyzer with a mass spectroscopy detector at a heating rate of 25 °C/min from 50 °C to 750 °C.

3 Results

3.1 Microstructural analysis

The initial microstructure of Alloy 718 after aging is shown in Fig. 2(a) with equiaxed grains and an average grain size of 73.5 μm. Annealing twins can be observed inside the grains, as highlighted by the yellow lines. Block-shaped nitrides (Nb, Ti)N and carbides (Nb, Ti)C are present in the matrix as illustrated in the EDS results, respectively. The coherent strengthening phases, spherical γ’ and disc γ’’, are homogeneously distributed in the matrix (Fig. 2(b)). A small fraction of the GBs is covered with needle-shaped

intermetallic precipitate delta (δ) phases, which extend into the matrix (Fig. 2(c)) and left with a precipitation-free zone (PFZ) due to the local depletion of Nb.

Fig. 2 Microstructure of Alloy 718 showing (a) carbides, (b) fine γ' and γ'' precipitates, and (c) the δ phase. (d) EDS information on incoherent (Nb, Ti)N nitrides and (Nb, Ti)C carbides.

3.2 Surface and subsurface response after electrochemical charging

The surface micrographs after charging are presented in Fig. 3, where we can see slip lines on the surfaces after charging. Besides, it was also possible to detect cracks on the surface after charging for more than 60 h (Fig. 3(c)–(g)). The entire formed cracks exhibit transgranular modes, as illustrated in Fig. 3(c1). Cracks larger than 15 $\mu m/mm^2$ started to form after charging the samples for more than 80 h. In severe cases, e.g., when the sample was hydrogenated for 168 h, its entire surface was filled with cracks with a tendency of peeling (Fig. 3(g)). As it is difficult to determine the exact number of cracks in this condition, the surface damage statistics excluding this case were characterized and summarized in Fig. 3(h); in this diagram, it can be observed that both the number density and the length density of surface cracks increase with charging time ($\geq$ 40 h). And there is a crack length jump at 80 h charging. In the current study, a time period of 40 h is set as the threshold for hydrogen-induced surface cracking.

Fig. 3 BSE images ((a)-(c)), and SE images ((d)-(g)) showing slip lines and surface cracks on Alloy 718 samples after electrochemical charging. The magnified view of the area highlighted by the dashed circle in (c) is shown in (c1). (h) Statistical summary of the crack number and crack length densities on the surfaces after charging from 20 h to 120 h.

Apart from the surface damage induced by electrochemical charging, subsurface damages were also studied in hydrogen-charged samples alone without the application of any mechanical loading. Subsurface cracks can be observed after 100 h of charging. Take 120 h charged condition as an example, we found that the crack cut through carbides in a transgranular mode inside the grain (Fig. 4(a)). The crack path follows {111} plane trace

(red dash lines in the slip traces in Fig. 4(b)) and exhibits a symmetric morphology across Σ3 annealing twin boundaries (TBs), but it is not deflected by carbides. The displacement and rotation of cracking attributes to their transmission through TBs. The formation of crack caused a large amount of plasticity, which results in a bulge on the surface (Fig. 4(a)) as shown by the kernel average misorientation (KAM) in Fig. 4(c). A misorientation of 2° to 8° is detected between the crack and the surface. When the crack reaches GBs, it is transmitted into another grain (Fig. 4(e)). However, the crack has a tendency to propagate along the GB which is decorated with precipitates (Fig. 4(d, d1)), and causes the debonding of δ phase-matrix interface.

Fig. 4 SEM and EBSD analysis of subsurface cracks in the 120 h charged sample. (a), (d), and (e) Micrographs illustrating crack paths. (b) ND-IPF (inverse pole figure) map and (c) KAM map of the crack. (d1) is the ND-IPF map of the area highlighted by the yellow box in (d). (TB: twin boundary, GB: grain boundary. The color scale of the IPF maps is shown in the IPF triangle. The color scale of the KAM map is shown in the color bar.)

3.3 Slow strain rate tensile testing

To further investigate the effect of pre-formed cracks on the mechanical behavior of Alloy 718, SSRT was conducted after surface characterization. The engineering stress-strain curves generated under different charging conditions are presented in Fig. 5(a). The 168 h-charged sample was not considered as the sample was severely damaged during charging. Fig. 5(b) shows that hydrogen decreases the ultimate tensile strength (UTS) due to the reduction of the total elongation (from 27.6% without hydrogen to 2.06% after 120 h of charging). The yield strength (YS), defined as 0.2% offset stress, increases with hydrogen charging up to 60 h, after which it reduces gradually to a value lower than the YS in air at 120 h. The embrittlement factor (EF) is defined as eq. (1) [31, 47] and its evolution with respect to the charging time is presented in Fig. 5(c). It describes the relative elongation loss of the hydrogenated samples in comparison to the non-charged samples.

$$\mathrm{EF} = \left(1 - \frac{\varepsilon_{\mathrm{H}}}{\varepsilon_{\mathrm{no\ H}}}\right) \times 100\% \quad (1)$$

where ε_H is the engineering strain of a precharged sample after fracture and $\varepsilon_{no\,H}$ represents the engineering strain of a hydrogen-free sample. The EF increases with charging time and becomes almost constant after 80 h of hydrogenation.

Fig. 5 (a) Engineering stress-strain curves of the tested specimens under different charging conditions. Effect of hydrogen on (b) 0.2 % YS and UTS (b) and (c) EF.

3.4 Fractography

Post mortem fractography characterization with and without hydrogen exposure was done after tensile tests. Fig. 6(a1)–(a2), (a4) show the fractography of hydrogen-free samples; the fracture surface exhibited microvoid coalescence (MVC)-assisted failure in a ductile fracture mode. Necking is a distinct feature of the ductile failure process (Fig. 6(a1)). Higher magnification images of carbonitride cracks and dimples are presented in Fig. 6(a2) and (a4). Micrographs in the vicinity of necking region show severely deformed grains with secondary cracks across carbonitrides (Fig. 6(a3)). Two activated slip systems revealed by ECCI are shown in Fig. 6(a5).

Conversely, the hydrogenated samples displayed a multi-mode failure process. A representative fracture surface of 20 h electrochemically charged sample is shown in Fig. 6(b1): it consists of a brittle area near the sample surface, a ductile region in the sample interior enclosed by the red dotted line, and a transition from brittle to ductile regions in between. In the brittle region, both intergranular and transgranular cracks are observed. Ridges, steps, and river patterns in the brittle region display transgranular features, and nanovoids along the GBs exhibit a tendency for intergranular cracking (Fig. 6(b2)). The steps and cleavage facets in Fig. 6(b3) show that dislocation slip preferred along certain slip planes. Nanovoids are observed at slip line intersections (Fig. 6(b4)). In addition, secondary transgranular cracks on the surface follow the direction of slip bands and exhibit zig-zag morphologies (Fig. 6(b5)). The same case as in the non-charged sample, most carbides on the surface are cracked.

Fig. 6 (a1)-(a5): Micrograph analysis of no-hydrogen sample after failure showing (a1, a4) ductile fracture features, (a2, a3) carbonitride cracks, and (a5) surface slip lines; (b1)-(b5): micrograph analysis of a fractured sample with 20 h-charging showing (b1) transition from brittle to ductile fracture, (b2) GB microvoids, (b3) transgranular steps, (b4) microvoids at slip lines intersections, and (b5) surface secondary cracks.

Percentage of brittle area (POB) is introduced to visualize the effect of hydrogenation time on the fracture mode and assess HE sensitivity:

$$\mathrm{POB} = \frac{A_T - A_D}{A_T} \times 100\% \quad (2)$$

where A_T is the total area of the fracture surface and A_D is the area of the ductile region. The results in Fig. 7(a) indicate an increase in POB with charging time. A drastic increase in POB happened between 60 and 80 h. After 120 h of charging, the fracture surface exhibits a fully brittle fracture mode. The corresponding brittle depths of the areas showing brittle fracture in each charging condition are summarized in Fig. 7(b), which are consistent with the changes in POB.

Fig. 7 Effect of hydrogen on (a) POB and (b) the corresponding brittle depth.

3.5 Subsurface crack analysis after loading

Subsurface cracks on three cross section layers were analyzed after loading the samples to fracture. In the non-charged sample, the subsurface shown in Fig. 8(a) exhibits cracks in the secondary-phase particles without intruding into the matrix, which is fully consistent with the fractography in Fig. 6(a1). In comparison, both intergranular and transgranular cracks are observed on the hydrogenated samples. Representative subsurface cracks with their ND-IPF maps are shown in Fig. 8(b)–(e). In accordance with previous studies [37, 48, 49], TBs show great resistance to crack propagation. An intergranular crack is deflected and a transgranular crack becomes blunted when they reach TBs as shown in Fig. 8(c).

Fig. 8 Micrographs of the cross sections of (a) a hydrogen-free sample showing carbides cracks. (b)-(c) BSE images and ND-IPF maps, respectively, of a hydrogen-charged sample showing both intergranular and transgranular cracks. (d)-(e) BSE images and ND-IPF maps, respectively, of a hydrogen-charged sample showing only intergranular cracks, step size: 0.2 μm.

For a statistic analysis of these cracks, we divide them into three categories: transgranular cracks, low-Σ (Σ = 1–29) [49], and general GB (all other GBs) cracks, as shown in Fig. 9(a). Only one subsurface crack is observed at 40 h of hydrogen charging and three at 60 h of the examined cross-sections. The total number of intergranular cracks remains almost constant after charging the samples for more than 80 h, while that of transgranular cracks increases drastically with respect to the charging time. Here we assumed that intergranular cracks originate from the nearest triple junctions to the surface, and transgranular cracks initiation points are measured by the distance from the surface to the nearest cracking point. Examples of the above measurements are highlighted by the yellow arrows in Fig. 8(b)–(d). Fig. 9(b) summarizes the results and indicates that most transgranular cracks are formed near free surfaces. For samples charged for 100 h and 120 h, half of the cracks connect to the surfaces. In comparison, intergranular cracks tend to nucleate deeper in the material matrix. For samples charged between 80 to 120 h, the outermost intergranular cracks occurr at an average distance of (21.50 ± 4.99) μm to the free surface, which is in agreement with the average outermost triple junction sites distance of (26.83 ± 4.56) μm. A detailed discussion of both transgranular and intergranular cracking will be presented in sections 4.3 and 4.4.

Fig. 9 Statistical analysis of subsurface cracks: (a) the number of different types of cracks on the cross-sections; and (b) distance between surface and cracks.

3.6 Slip transferability at GBs

Take a close look at the intergranular cracks and to understand the cracking mechanism in a new perspective, 3D information of GBs was collected using FIB cross section milling technique. Basically, in the STRONG model, a GB is described by two pairs of Euler

angles (φ1 Φ φ2) in adjacent grains and two angles (η, ε) determining the direction of GB, as illustrated in Fig. 10. The resistance of GB to slip transmission can be expressed as eq. (3) [37]:

$$\omega_{ij} = 1 - \cos\alpha_{ij} \cdot \cos\beta_{ij} \quad (3)$$

where α is the angle between the intersection lines of the active slip plane in each grain with the GB and β is the angle between the corresponding slip directions in adjacent grains. A schematic of the residual Burges vector $\overrightarrow{b_r}$ is defined by the difference of Burgers vector of both slip systems. The matrix ω_{ij} contains in total 144 single slip systems couplings, which yield a comprehensive description of the GB resistance to slip transmission. Fig. 11 shows two examples of GB cracks and the necessary parameters needed for ω calculation. The depth tilt angle ε can be obtained from the cross sections of the GBs (Fig. 11(a3) and (b4)). To measure the surface trace angle η, the direction parallel to the gauge length was used as the reference line. The {111} slip traces are marked in Fig. 11(a2) and (b2)–(b3) with different colors indicating Schmid factor (SF) variation from the highest to the lowest value (red-blue-light blue-dark). The active slip systems can be determined by comparing the SFs with {111} slip traces that were unambiguously measured by ECCI (Fig. 11(a2) and (b2)–(b3)), and they are marked by dot lines.

Fig. 10 Schematic of slip system coupling at a GB, together with GB traces, represented by angles (η, ε).

Fig. 11 ND-IPF maps (a) (b), and corresponding SE images (a1) and (b1) showing GB cracks. The ECC micrographs (a2) (b2)-(b3) indicate active slip lines that represent {111} traces (the magnitude of Schmid factors varies from the highest to the lowest value: red, blue, light blue, black; the active slip planes are marked in dotted lines), (b2)-(b3) are magnified ECC images of areas in (b1) that are marked in yellow. (a3) (b4) The FIB cross sections show GB depth tilt angles.

A summary of the measured GB parameters (including GB misorientation axes and angles), calculated SFs, GB resistance on several cracked GBs (C-GBs) of a sample that fractured after hydrogen charging is presented in Table 2. Non-cracked GBs (NC-GBs) next to the C-

GBs, which are assumed to have similar stress level as those C-GBs, are presented as well. Since low-Σ GBs are relatively resistance to cracking compared to general GBs, we focused only on general GBs for the current study. The highest SF for each slip plane was calculated and presented in Table 2. The analyzed C-GBs and NC-GBs are in the range of high misorientation angles. For each of the grains adjacent to the GB, at least two slip planes were activated. When the divergence between the intersection lines of active slip planes with the GBs (α angle) is lower than 15°, there is a higher probability of slip transferability [50]. All the NC-GBs shown in Table 2 have at least one coupling slip plane with relatively low α (≤15°). In comparison, α angles of the C-GBs are much higher, with only one exception (gA-3/gB-3). Also, the parameter representing the resistance of GB to slip transmission, ω, for C-GBs are higher than those for NC-GBs. This indicates that, in the presence of hydrogen, GBs that possess low slip transmission have high stress incompatibility and can initialize crack easily.

Table 2 Measured GB parameters, active slip planes with corresponding SFs, and GB resistance calculated from eq. (3). (U V W)/ θ represents the misorientation axis and angle between adjacent grains.

4 Discussion

The aim of this study is to perform a systematic hydrogen charging process to analyze the impact of electrochemical charging alone on the microstructure change of Alloy 718, and the relation between hydrogen-induced pre-damages and the cracking behaviors in the process of mechanical loading. In the discussion part, firstly hydrogen concentration profile along the sample was calculated to help explain the hydrogen-induced slip lines and cracks during hydrogen adsorption. Subsequently, the possible reasons for transgranular cracking and intergranular cracking were discussed in detail.

4.1 Pre-damages induced by cathodic charging

The results presented above show that slip lines were formed on the surface of Alloy 718 followed by surface and subsurface cracking in the process of electrochemical charging.

These phenomena were rarely detected and documented. The most probable reason for not being able to detect them can be attributed to the surface condition after charging, which exhibits a relatively high surface roughness or corrosion. In the present study, the sample surface was electropolished before hydrogen charging to guarantee a surface with no residual stress and the usage of a glycerol-based electrolyte ensured surface integrity. Therefore, the microstructure change on the sample in the process of cathodic charging could be recorded. The formation of surface and subsurface cracks shows severe damage caused by hydrogen ingress alone. Due to a low hydrogen diffusivity in Alloy 718, it is reasonable to infer that a gradient in hydrogen concentration from the edge to the inner region is developed with the highest concentration at the surface. And the internal stress due to hydrogen distribution inhomogeneity plays a crucial role. To visualize hydrogen concentration distribution during different charging time, the plane sheet diffusion model [51] with a fixed diffusion coefficient was used. In this context, we need to solve the one-dimensional form of Fick's second law, which is represented by eq. (4):

$$\frac{\partial \mathrm{C}}{\partial \mathrm{t}} = \mathrm{D}\frac{\partial^2 \mathrm{C}}{\partial^2 \mathrm{x}} \tag{4}$$

where C is the hydrogen concentration at a specific time t and distance x from the center of the specimen along the thickness direction. D is the hydrogen diffusion constant, which is independent of hydrogen concentration and local stress state, and can be calculated as eq. (5) [52]:

$$\mathrm{D} = 4.06 \times 10^{-7} \exp\left(-\frac{48.63\mathrm{kJ}\,/\,\mathrm{mol}}{\mathrm{RT}}\right) \mathrm{m}^2/\mathrm{s} \tag{5}$$

where R is the gas constant, and T is the charging temperature (348.15 K in the present study). This yields the value of D 2.05×10^{-14} m^2/s. Considering that the specimen is symmetric at x = 0 in the center, the boundary conditions in the region of $-L \leq x \leq L$ (L equals half length of the thickness) for this equation can therefore be written as eqs. (6)-(8):

$$\mathrm{C} = \mathrm{C}_0, \mathrm{x} = \mathrm{L}, \mathrm{t} \geq 0 \tag{6}$$

$$\mathrm{C} = \mathrm{C}_0, \mathrm{x} = -\mathrm{L}, \mathrm{t} \geq 0 \tag{7}$$

$$\frac{\partial C}{\partial x} = 0, x = 0, t \geq 0 \tag{8}$$

where C_o is the concentration of hydrogen adsorbed at the surface. Assuming that hydrogen concentration in the specimen before charging is 0 and use Laplace transformation, the solution of eq. (4) can be expressed as eq. (9):

$$\frac{C}{C_o} = \sum_{n=0}^{\infty} (-1)^n \operatorname{erfc} \frac{(2n+1)L - x}{2\sqrt{Dt}} + \sum_{n=0}^{\infty} (-1)^n \operatorname{erfc} \frac{(2n+1)L + x}{2\sqrt{Dt}} \tag{9}$$

The solution of eq. (9) is schematically shown in Fig. 12(a) in section 4.2. The calculated hydrogen concentration ratio terminates at different points, corresponding to a variation in samples' thickness. Obviously, a steep concentration gradient is generated along the sample, which is a common feature in FCC metals during cathodic charging [30, 53, 54]. In this alloy, the aging process annealed out most of the internal stress induced by water quenching, and electropolishing before hydrogen charging guaranteed the surfaces free from residual stresses. By hydrogen charging, the lattice expands, and stress evolves in the crystal. As soon as the stress reaches the level required for activation of dislocations, dislocation loops are emitted to accommodate the strain gradient in the sample and those dislocations can be assumed to be geometrically necessary dislocations (GND). Besides, the introduction of hydrogen can reduce the dislocation line energy, which further contributes to the activation of Frank-Read source [55-57]. And a high supersaturation of hydrogen accompanied by the high stresses near the surface [12] act as a driving force for dislocations to slip and leave slip traces at free surfaces (Fig. 3). This phenomenon was also reported in an austenitic phase of a super duplex stainless steel during in-situ electrochemical hydrogen charging [55]. It is also reasonable to infer that, at longer hydrogen charging time, cracks on the surface can generate at slip band intersections where stress concentration is high (Fig. 3(c1)). A similar process occurred during the pulsed plasma nitriding (PPN) of austenitic stainless steel [58]; in that case, the nitrogen content across the PPN layer was measured using an electron probe micro-analyzer, which is responsible for the observed dislocation density gradient. However, in the present study, a direct measurement of hydrogen content along the sample was difficult due to the limitations of achieving resolution within the available techniques.

It was previously proposed that subsurface cracks are caused by the accumulation of hydrogen atoms at microscopic defects, such as voids, second phase particles, and grain boundaries [59]. However, a recent study by Griesche et al. [60] stated that the presence of a second phase is not a prerequisite for cracks formation. And no hydrogen segregation was detected at the interfaces of carbonitrides by using Nanoscale Secondary Iron Mass Spectrometry [29]. In this case, hydrogen-induced subsurface cracks could be related to hydrogen segregation at pre-existing voids or grain boundaries. Meanwhile, hydrogen-induced cracking with a noticeable opening displacement beneath the surface were reported to be caused by surface blisters [39-41, 61]. However, most of the studies were on body-centered cubic (BCC) metals. Only one paper mentioned the hydrogen-induced blister on aluminum alloys [62], but subsurface characterization was not performed. Moreover, none of these studies reported the formation of slip traces on the surface before blister formation. To determine whether such internal crack (Fig. 4) is a hydrogen-induced blister or not, hydrogen fugacity inside the crack and on the surface was discussed. On one hand, assuming that the internal gas pressure P_{H_2} at the internal cavity that was caused by the recombination of hydrogen atoms into hydrogen molecules around the defects can be roughly estimated from eq. (10) [63]:

$$P_{H_2} = \frac{K_{IC}\sqrt{\pi}}{2\sqrt{a}} \tag{10}$$

where K_{IC} is the fracture toughness of Alloy 718 alloy (95.8 $MPa\sqrt{m}$) [64] and a is the radius of the crack, which is assumed to be half size of the crack length. Here we chose the 120 h-charged sample for an estimation of the internal hydrogen pressure. This yields P_{H_2} the value of 8.5 GPa. And the hydrogen fugacity in the cavity can be calculated by using the Abel-Noble equation (eq. (11)) [65]:

$$f = P_{H_2} \cdot \exp\left(P_{H_2}\frac{b}{RT}\right) \tag{11}$$

where $b = 1.584 \cdot 10^{-5} m^3 mol^{-1}$, and this results in the extremely high values of f (order of 10^{25} atm). On the other hand, the hydrogen fugacity on the sample surface f_s is

proportional to the hydrogen surface concentration C_0 during electrochemical charging, as described by the Sivert's law [66]:

$$C_0 = S_H\sqrt{f_s} \tag{12}$$

where S_H is the solubility limit of hydrogen during charging, which can be measured from eq. (13) [67]:

$$S_H = 8.8 \cdot \exp\left(\frac{-8.1\ \mathrm{kJ/mol}}{RT}\right) \mathrm{wt\ ppm\ H}/\sqrt{\mathrm{atm}} \tag{13}$$

And the hydrogen surface concentration can be estimated from the total hydrogen concentration in the sample C_M by using eq. (14) [68]:

$$C_0 = \frac{\omega C_M}{4}\sqrt{\frac{\pi}{Dt}} \tag{14}$$

where ω equals to the sample thickness. As shown in Fig. 3, 20 h is the least hydrogen charging time that can generate slip lines on the surface without causing any surface and subsurface damages. Therefore, TDS test has been performed after the sample was hydrogenated for 20 h, which yields C_M as 36.5 wt. ppm. The corresponding hydrogen surface concentration C_0 and the hydrogen fugacity f_s yield the values of 189.4 wt. ppm and 1.2×10^5 bar, respectively. The huge difference between hydrogen fugacity in the cavity and on the surface indicates that the internal crack generated during cathodic charging is not a high internal pressure-induced blister. If the blister formation were assumed, the hydrogen fugacity in the cavity and on the surface should be in a comparable level due to the continuous equilibrium of the hydrogen activities near to the surface. Thus, it is reasonable to infer that these cracks were initiated at stress concentrated areas such as GBs and TBs due to the formation of internal stress during charging.

To substantiate that the surface slip lines and cracks are caused by the internal stress due to hydrogen distribution inhomogeneity along the sample, the internal stress σ is calculated and compared with the critical resolved shear stress (CRSS) for dislocation slip. The internal stress induced by abundant dissolved hydrogen can be estimated by eq. (15):

$$\sigma = B \cdot \frac{\Delta V}{V_0} \quad (15)$$

where B is the bulk modulus of Alloy 718, and $\Delta V/V_0$ is the lattice volume change by hydrogen. The value of B cannot be obtained directly from the literature, however, one can estimate it from the bulk modulus of γ'' phase (211 GPa) and γ' phase (229 GPa) in Inconel 718 [69]. In addition, the lattice expansion $\Delta V/V_0$ has a linear relationship with the dissolved hydrogen [70]:

$$\frac{\Delta V}{V_0} = \frac{H_a}{M_a}\frac{\Delta \nu}{\Omega} \quad (16)$$

where H_a/M_a represents the atomic ratio between hydrogen and metal near to the surface during charging, Δν is the volume change per hydrogen atom, and Ω is the mean volume of metal atom. For Ni, this ratio was reported as 0.28 [71]. The atomic ratio H_a/M_a can be calculated by eq. (17):

$$H_a/M_a = \frac{C_0 \times N_A/M_H}{(10^6 - C_0) \times N_A/M_A} \quad (17)$$

Where N_A is the Avogadro constant, M_H and M_A are the molar mass of hydrogen (1 g/mol) and the studied Alloy 718 (59.5 g/mol), respectively. As a result, the internal stress σ near to the surface in 20 h charging condition yields 665.7 MPa. This value is higher than the CRSS (218.9 MPa) for slip in a single crystal that is deduced from the measured polycrystalline yield stress σ_Y (669.8 MPa for 20 h charging) using the Taylor factor (3.06) [72]. The above calculations confirm that the internal stress generated during electrochemical charging is high enough to be the driving force for the hydrogen-induced surface damages. Worthy of note, the estimated value of the internal stress, which is only an approximation based on the Hook's law, though not accurate, is able to qualitatively testify the mechanism for the plastic deformation during hydrogen charging. This deduction also applies to the longer time charging conditions.

4.2 Failure mode of Alloy 718 with the presence of hydrogen

The deformation mechanism in hydrogen-charged samples is different from that of hydrogen-free samples. The failure mode of Alloy 718 transfers from ductile to brittle fracture. Both transgranular and intergarnular fracture modes were found on samples failed in a hydrogenation environment. By introducing hydrogen, YS increased at first due to the solid solution strengthening effect of hydrogen, which was also reported for iron [73] and FCC high-entropy alloys [74, 75]. During the increment of charging time, YS after 80 h charging reduced, which might be caused by the internal and external pre-damages generated during hydrogen charging (Fig. 3). This resulted in a rapid fracture after reaching the yield point. At the same time, there is a drastic change of EF and POB results between 60 and 80 h (Fig. 7(a)), which fits well with the sudden increment in surface crack length density after charging (Fig. 3(h)), indicating again that pre-damages induced by cathodic charging assist both the formation and growth of cracks in the process of mechanical loading. Once a pre-crack is large enough, it propagates readily at a lower stress level, which results in the early brittle fracture of the sample.

It is worth mentioning that the brittle depth at each charging condition measured from fractography corresponds well to the hydrogen concentration at approximately 0.12 C_0 (Fig. 12 (a)) that obtained from the simulation, as illustrated in Fig. 12(b). This result means that the sample region with a hydrogen concentration reaches to this level (22.7 wt. ppm) during electrochemical charging can cause a brittle fracture upon mechanical loading. Although hydrogen charging solution in Ref. [67] is different from the current study, the usage of both acidic electrolytes can, to some extent, give a hint for the amount of hydrogen that can initiate brittleness.

Fig. 12 (a) Hydrogen concentration profile for different charging time and (b) comparison of hydrogen effect on brittle depth measured from fracture surface and the simulated 0.12 C_0 results.

4.3 Hydrogen-assisted transgranular cracking during deformation

Concentration gradient during hydrogen charging results in compressive stresses in the outer regions of the sample [12], which in turn causes slip lines and surface/subsurface

cracks even without mechanical loading. Once the sample is loaded, those pre-damages can easily propagate with the assistance of hydrogen accumulated at these stress concentration regions. Since part of the transgranular cracks were surface cracks, and there is a drastic increment of transgranular cracks between 80 h and 120 h (Fig. 9(a)) even though they fractured at similar deformation level, it is reasonable to infer that surface cracks induced by hydrogen charging promoted the formation and propagation of transgranular cracks. Concomitantly, intersections of slip lines act as strain concentration areas that attract hydrogen, and the formation of embryos of nanovoids becomes easier (Fig. 6(b4)) [8, 28, 30]. Quasi-cleavage is a commonly reported fracture feature in the hydrogenated precipitation-hardened Alloy 718 [9, 29, 76, 77]. Hydrogen-induced cracking along dislocation slip bands (DSBs), particularly at nonparallel DSBs intersections near the surface [8, 9, 76], has been claimed to be the reason for the observed quasi-cleavage feature. Hydrogen atmospheres reduce the tendency for dislocation cross-slip by stabilizing the edge component [78]. Furthermore, the reduction of SFE due to the presence of hydrogen [68, 79, 80] promotes slip planarity and enhances the stress concentration at the intersections of {111} slip planes. In the current study, another possible reason for the occurrence of surface transgranular cracking upon loading is the difference in the stress conditions between surfaces and subsurfaces. At regions close to the surface where plane stresses dominate, grains experience relatively lower incompatibility stresses and constraints from neighbouring grains. Thus, surface GBs are tougher and show less cracking compared to the grain interior. This in return promotes the possibility of transgranular cracking on the surface. To the authors' knowledge, this is for the first time to report that hydrogen charging alone causes slip lines and cracks in nickel-based superalloys. It is worth mentioning that the charging condition is relatively moderate and without any hydrogen poison. Compared to the room temperature (25 °C), the current charging temperature (75 °C) increases the hydrogen diffusion rate and solubility by 16.7 and 1.6 times, respectively, according to eqs. (5) and (13). Thus, one would expect a more severe hydrogen charging condition with a steeper hydrogen concentration gradient at room temperature. Compared to pure Ni and other nickel-based alloys showing intergranular failure, the pronounced transgranluar fracture in the tested Alloy 718 could be attributed to

several reasons. It was reported that the failure mode of Alloy 718 is highly dependent on the virgin microstructure [7, 8, 30]. When the GBs are heavily decorated with δ phase, intergranular failure is more frequently observed, which is not the case in the current material with merely small fraction of δ phase. Additionally, hydrogen-induced internal stress initiates dislocation slips and possible transgranular cracks with prolonged charging time. Those pre-damages act as pre-existing stress concentrators that can substantially promote transgranular cracking upon loading. Moreover, the pronounced localized planar slip due to the high volume of nano-sized precipitates facilitates the slip planes as the sources of cracks rather than the GBs. With mechanical loading, transgranular crack evolves more, albeit both types of cracks are evolving. The results showed that hydrogen-charging induced pre-damages had a detrimental effect on the mechanical behavior of nickel-based superalloys. And it is necessary to consider this effect on HE in future experimental studies.

4.4 Hydrogen-assisted intergranular cracking during deformation

Hydrogen-assisted intergranular cracking was observed in the precipitation hardened nickel-based superalloys. Different from the debonding mechanism proposed for intergranular cracking in the presence of δ phase [28, 30, 53], in this study, we introduced a new parameter, i.e. GB resistance to slip transmission, to understand the stress incompatibility between the adjacent grains and its impact on the propensity for GB cracking. In general, GBs will block dislocations from intragranular movement and enhance local stress incompatibility, which in turn increases the risk of crack initiation [81]. The transferability of slip systems through GBs has been proved to play a crucial role in the evaluation of local GB flow stress in pure Ni [82] and GB crack initiation in mild steels [43]. To predict which slip system is favorable for slip transfer, Lee, Robertson and Birnbaum [83] proposed three criteria: (a) the angle between the intersection lines of the slipping planes with the GB plane should be minimal; (b) the component of the residual Burgers vector that protrudes from the grain boundary should be minimal; (c) the resolved shear stress acting on the active slipping system should be maximum. The introduction of

GB resistance to slip transmission, ω_{ij}, provides the possibility of describing dislocations transferability at GBs by considering conditions (a) and (b). Condition (c) is not so easy to determine due to the superimposed local stress caused by the anisotropic elastic incompatibility of the two neighbouring grains. The normalized effective normal stress acting on a GB can be described by the Schmid-Modified Grain Boundary Stress (SMGBS) model [84]. However, it does not provide quantitative results, but rather an indication of the stress field variation with a discrepancy in grain orientations. Meanwhile, one should consider the synergetic effect of all these factors, since the slip system experiencing the maximum resolved shear stress need not be activated if conditions (a) and (b) are not satisfied [85]. In the current study, we focused on conditions (a) and (b), which are more important when more than one active incoming or outgoing slip system operates. Assuming that the critical value for ω_{ij} is $\omega = 1 - \cos 15° \cdot \cos 15° = 0.067$, which is in line with the suggestions made by Davis [50] and Werner [86], it is quite obvious that in the hydrogen-charged samples, ω_{ij} of C-GBs is much higher than the critical value (Table 2). This means that the transferability of slip at those GBs is much more difficult, and a high stress incompatibility will arise at those regions. An intuitive example of the non-transferrable slip is the high flow stress and local buckling at GBs due to dislocation pile-ups, which was reported on the deformed high-angle GB bi-crystal micropillars [82]. Furthermore, molecular dynamic simulations of iron in Ref. [87] claimed that hydrogen atoms segregating along the GB distort the lattice structure, thus consistently increase the energy barrier to slip transmission. Meanwhile, slip planarity is enhanced in FCC metals in the presence of hydrogen owing to the reduction of SFE [79, 80]. Hence, local flow stress increases at the intersections of GBs with {111} sliding planes. The accumulation of hydrogen atoms at those stress concentration areas further reduces the defect-formation energy in the framework of "the Defactant" model proposed by Kirchheim [57, 88]. As a result, cracks occur readily. On the other hand, the GB resistance of NC-GBs is very close to the critical value, which indicates that a slip can pass through more easily in those GBs with higher microscopic compatibility. It is worth mentioning that all the analyzed GBs in Table 3 are free of δ phase, which eliminates the detrimental effect of δ phase when assessing slip transferability at GBs. The δ phase was proposed to exert a nontrivial effect

on the intergranular GB cracking by initializing micro-cracks [28, 29], since a soft PFZ around δ enhances stress localization. In addition to avoiding the formation of the δ phase through optimizing the heat treatment processes, attention should also be paid on how to achieve GBs that hold high slip transferability in the concept of GB engineering.

5. Conclusions

Hydrogen embrittlement in electrochemically charged Alloy 718 was investigated using slow strain rate tensile test (SSRT) in combination with advanced characterization techniques, i.e. secondary electron microscopy (SEM), electron channeling contrast imaging (ECCI), electron backscattered diffraction (EBSD), and electron dispersive spectroscopy (EDS). Focused ion beam (FIB) was used to collect 3D information of GBs. A systematic study was conducted on the impact of hydrogen charging on the alloy's microstructure change and its mechanical properties during mechanical loading. The transgranular cracking mechanism was discussed in detail by calculating hydrogen concentration profiles. In this study, GB compatibility, i.e., dislocation slip transferability was considered for the first time to explain the intergranular fracture in nickel-based superalloys by using STRONG model. The major conclusions can be summarized as:

1) The presence of hydrogen has a strong detrimental effect on the mechanical properties of Alloy 718; the mechanical property degradation is accompanied by a transition from microvoid coalescence (MVC)-induced ductile failure to hydrogen-assisted brittle fracture. Both transgranular and intergranular cracks could be observed. In the current material, sample regions with a hydrogen concentration reaches to 22.7 wt. ppm during electrochemical charging can initiate brittleness upon mechanical loading.
2) Electrochemical charging has a prominent effect on the cracking behavior of Alloy 718. Cathodic charging alone caused slip lines, surface and subsurface cracks. The formation of pre-damages results in a reduction of yield strength, an increment of embrittlement factor and percent of brittle area, and finally assists an early failure of the alloy. Hydrogen concentration gradient accompanied by the high stresses near

the surface is responsible for the initiation of the pre-damages. These damages are cracking sources in the process of mechanical loading.

3) The formation of transgranular cracks resides in two reasons: (a) pre-damages caused by electrochemical charging before loading promoted the initiation and propagation of transgranular cracks; (b) intersections of dislocation slip bands on {111} planes act as stress concentrators that attract hydrogen and lead to void nucleation, which finally results in cracking.
4) The GB transferability of dislocations is an important factor determining the propensity for intergranular cracking. In the presence of hydrogen, GBs with high resistance to slip transmission increases the probability for crack initiation upon loading due to the synergetic effect of hydrogen and local stress incompatibility, and GBs with lower resistance to slip transmission are less susceptible to cracking.

Acknowledgements

The authors gratefully acknowledge the financial support from the Research Council of Norway through the project HyF-Lex (244068/E30). Aker Solutions is acknowledged for providing Alloy 718. The Research Council of Norway is acknowledged for the support to the Norwegian Micro- and Nano-Fabrication Facility, NorFab, project number 245963/F50.

References

[1] N. Totsuka, E. Lunarska, G. Cragnolino, Z. Szklarskasmialowska, Effect of hydrogen on the intergranular stress-corrosion cracking of Alloy-600 in high-temperature aqueous environments, Corrosion 43(8) (1987) 505-514.
[2] Y. Yao, X.L. Pang, K.W. Gao, Investigation on hydrogen induced cracking behaviors of Ni-base alloy, Int. J. Hydrog. Energy 36(9) (2011) 5729-5738.
[3] P.D. Hicks, C.J. Altstetter, Internal hydrogen effects on tensile properties of iron-base and nickel-base superalloys, Metall. Mater. Trans. A 21(2) (1990) 365-372.
[4] A.M. Brass, J. Chene, Influence of deformation on the hydrogen behavior in iron and nickel base alloys: a review of experimental data, Mater. Sci. Eng. A 242(1-2) (1998) 210-221.
[5] J. Chene, A.M. Brass, Role of temperature and strain rate on the hydrogen-induced intergranular rupture in alloy 600, Metall. Mater. Trans. A 35a(2) (2004) 457-464.

[6] A. Kimura, H.K. Birnbaum, Hydrogen induced grain-boundary fracture in high-purity nickel and its alloys - enhanced hydrogen diffusion along grain-boundaries, Acta Metall. 36(3) (1988) 757-766.
[7] Z. Tarzimoghadam, M. Rohwerder, S.V. Merzlikin, A. Bashir, L. Yedra, S. Eswara, D. Ponge, D. Raabe, Multi-scale and spatially resolved hydrogen mapping in a Ni–Nb model alloy reveals the role of the δ phase in hydrogen embrittlement of alloy 718, Acta Mater. 109 (2016) 69-81.
[8] Z.B. Zhang, G. Obasi, R. Morana, M. Preuss, Hydrogen assisted crack initiation and propagation in a nickel-based superalloy, Acta Mater. 113 (2016) 272-283.
[9] Z. Zhang, G. Obasi, R. Morana, M. Preuss, In-situ observation of hydrogen induced crack initiation in a nickel-based superalloy, Scr. Mater. 140 (2017) 40-44.
[10] W.H. Johnson, On some remarkable changes produced in iron and steel by the action of hydrogen and acids, Proc. Royal Soc. Lond. 23 (1875) 168-179.
[11] S.P. Lynch, Environmentally assisted cracking - overview of evidence for an adsorption-induced localized-slip process, Acta Metall. 36(10) (1988) 2639-2661.
[12] H.K. Birnbaum, P. Sofronis, Hydrogen-enhanced localized plasticity - a mechanism for hydrogen-related fracture, Mater. Sci. Eng. A 176(1-2) (1994) 191-202.
[13] A. Tehranchi, W.A. Curtin, Atomistic study of hydrogen embrittlement of grain boundaries in nickel: II. Decohesion, Model. Simul. Mater. Sci. Eng. 25(7) (2017).
[14] H.K. Birnbaum, Mechanisms of hydrogen related fracture of metals, Illinois University at Urbana department of materials science and engineering, 1989.
[15] Y. Jagodzinski, H. Hanninen, O. Tarasenko, S. Smuk, Interaction of hydrogen with dislocation pile-ups and hydrogen induced softening of pure iron, Scr. Mater. 43(3) (2000) 245-251.
[16] L.B. Pfeil, The effect of occluded hydrogen on the tensile strength of iron, Proc. Royal Soc. Lond. 112 (1926) 182-195.
[17] W.W. Gerberich, R.A. Oriani, M.J. Lii, X. Chen, T. Foecke, The necessity of both plasticity and brittleness in the fracture thresholds of iron, Philos. Mag. A 63(2) (1991) 363-376.
[18] C.J. McMahon, Hydrogen-induced intergranular fracture of steels, Eng. Fract. Mech. 68(6) (2001) 773-788.
[19] S. Lynch, Hydrogen embrittlement phenomena and mechanisms, Corros. Rev. 30(3-4) (2012) 90-130.
[20] S.P. Lynch, Metallographic contributions to understanding mechanisms of environmentally assisted cracking, Metallography 23(2) (1989) 147-171.
[21] S.P. Lynch, Comments on "A unified model of environment-assisted cracking", Scr. Mater. 61(3) (2009) 331-334.
[22] S.P. Lynch, Mechanisms of hydrogen-assisted cracking, Metals Forum 2(3) (1979) 189-200.
[23] M. Nagumo, Hydrogen related failure of steels - a new aspect, Mater. Sci. Technol. 20(8) (2004) 940-950.
[24] Y. Yao, X. Pang, K. Gao, Investigation on hydrogen induced cracking behaviors of Ni-base alloy, Int. J. Hydrog. Energy 36(9) (2011) 5729-5738.
[25] S. Hinotani, Y. Ohmori, F. Terasaki, Effect of nickel on hydride formation and hydrogen embrittlement in Ni-Cr-Fe alloys, Mater. Sci. Eng. 74(2) (1985) 119-131.

[26] O.A. El kebir, A. Szummer, Comparison of hydrogen embrittlement of stainless steels and nickel-base alloys, Int. J. Hydrog. Energy 27(7-8) (2002) 793-800.
[27] L. Xiao, D.L. Chen, M.C. Chaturvedi, Shearing of γ″ precipitates and formation of planar slip bands in Inconel 718 during cyclic deformation, Scr. Mater. 52(7) (2005) 603-607.
[28] Z. Tarzimoghadam, D. Ponge, J. Klower, D. Raabe, Hydrogen-assisted failure in Ni-based superalloy 718 studied under in situ hydrogen charging: The role of localized deformation in crack propagation, Acta Mater. 128 (2017) 365-374.
[29] Z.B. Zhang, K.L. Moore, G. McMahon, R. Morana, M. Preuss, On the role of precipitates in hydrogen trapping and hydrogen embrittlement of a nickel-based superalloy, Corros. Sci. 146 (2019) 58-69.
[30] V. Demetriou, J.D. Robson, M. Preuss, R. Morana, Study of the effect of hydrogen charging on the tensile properties and microstructure of four variant heat treatments of nickel alloy 718, Int. J. Hydrog. Energy (2017).
[31] S. Jothi, S.V. Merzlikin, T.N. Croft, J. Andersson, S.G.R. Brown, An investigation of micro-mechanisms in hydrogen induced cracking in nickel-based superalloy 718, J. Alloys Compd. 664 (2016) 664-681.
[32] T. Watanabe, An approach to frain-boundary design for strong and ductile polycrystals, Res. Mech. 11(1) (1984) 47-84.
[33] T. Watanabe, S. Tsurekawa, The control of brittleness and development of desirable mechanical properties in polycrystalline systems by grain boundary engineering, Acta Mater. 47(15-16) (1999) 4171-4185.
[34] S. Bechtle, M. Kumar, B.P. Somerday, M.E. Launey, R.O. Ritchie, Grain-boundary engineering markedly reduces susceptibility to intergranular hydrogen embrittlement in metallic materials, Acta Mater. 57(14) (2009) 4148-4157.
[35] E.O. Hall, The Deformation and Ageing of Mild Steel .2. Characteristics of the Luders Deformation, Proc. Phy. Soc. B 64(381) (1951) 742-747.
[36] N.J. Petch, The Cleavage Strength of Polycrystals, J. Iron Steel Inst. 174 (1953) 25-28.
[37] A.F. Knorr, M. Marx, F. Schaefer, Crack initiation at twin boundaries due to slip system mismatch, Scr. Mater. 94 (2015) 48-51.
[38] M.D. Sangid, H.J. Maier, H. Sehitoglu, The role of grain boundaries on fatigue crack initiation - An energy approach, Int. J. Plasticity 27(5) (2011) 801-821.
[39] A. Laureys, E. Van den Eeckhout, R. Petrov, K. Verbeken, Effect of deformation and charging conditions on crack and blister formation during electrochemical hydrogen charging, Acta Mater. 127 (2017) 192-202.
[40] D. Pérez Escobar, C. Miñambres, L. Duprez, K. Verbeken, M. Verhaege, Internal and surface damage of multiphase steels and pure iron after electrochemical hydrogen charging, Corros. Sci. 53(10) (2011) 3166-3176.
[41] S. Ayadi, Y. Charles, M. Gaspérini, I. Caron Lemaire, T. Da Silva Botelho, Effect of loading mode on blistering in iron submitted to plastic prestrain before hydrogen cathodic charging, Int. J. Hydrog. Energy 42(15) (2017) 10555-10567.
[42] C.F. Dong, Z.Y. Liu, X.G. Li, Y.F. Cheng, Effects of hydrogen-charging on the susceptibility of X100 pipeline steel to hydrogen-induced cracking, Int. J. Hydrog. Energy 34(24) (2009) 9879-9884.

[43] W. Schaf, M. Marx, A.F. Knorr, Influence of microstructural barriers on small fatigue crack growth in mild steel, Int. J. Fatigue 57 (2013) 86-92.
[44] R. Kirchheim, Hydrogen Solubility and Diffusivity in Defective and Amorphous Metals, Prog. Mater. Sci. 32(4) (1988) 261-325.
[45] T. Hajilou, M.S.B. Hope, A.H. Zavieh, N. Kheradmand, R. Johnsen, A. Barnoush, In situ small-scale hydrogen embrittlement testing made easy: An electrolyte for preserving surface integrity at nano-scale during hydrogen charging, Int. J. Hydrog. Energy 43(27) (2018) 12516-12529.
[46] J.J.M. Jebaraj, D.J. Morrison, I.I. Suni, Hydrogen diffusion coefficients through Inconel 718 in different metallurgical conditions, Corros. Sci. 80 (2014) 517-522.
[47] L. Fournier, D. Delafosse, T. Magnin, Cathodic hydrogen embrittlement in alloy 718, Mater. Sci. Eng. A 269(1-2) (1999) 111-119.
[48] T. Watanabe, The impact of grain-boundary-character-distribution on fracture in polycrystals, Mater. Sci. Eng. A 176(1-2) (1994) 39-49.
[49] M. Seita, J.P. Hanson, S. Gradecak, M.J. Demkowicz, The dual role of coherent twin boundaries in hydrogen embrittlement, Nat. Commun. 6 (2015).
[50] K.G. Davis, Teghtsoo.E, A. Lu, Slip Band Continuity across Grain Boundaries in Aluminum, Acta Metall. 14(12) (1966) 1677-1684.
[51] J. Crank, The Mathematics of Diffusion, 2nd ed., Clarendon, Oxford, 1975.
[52] J. Xu, X.K. Sun, Q.Q. Liu, W.X. Chen, Hydrogen permeation behavior in In718 and Gh761 superalloys, Metall. Mater. Trans. A 25(3) (1994) 539-544.
[53] V. Demetriou, J.D. Robson, M. Preuss, R. Morana, Effect of hydrogen on the mechanical properties of alloy 945X (UNS N09945) and influence of microstructural features, Mater. Sci. Eng. A 684 (2017) 423-434.
[54] D. Wang, X. Lu, Y. Deng, X. Guo, A. Barnoush, Effect of hydrogen on nanomechanical properties in Fe-22Mn-0.6C TWIP steel revealed by in-situ electrochemical nanoindentation, Acta Mater. 166 (2019) 618-629.
[55] A. Barnoush, M. Zamanzade, H. Vehoff, Direct observation of hydrogen-enhanced plasticity in super duplex stainless steel by means of in situ electrochemical methods, Scr. Mater. 62(5) (2010) 242-245.
[56] R. Kirchheim, Reducing grain boundary, dislocation line and vacancy formation energies by solute segregation II. Experimental evidence and consequences, Acta Mater. 55(15) (2007) 5139-5148.
[57] A. Pundt, R. Kirchheim, Hydrogen in metals: Microstructural aspects, Annu. Rev. Mater. Res. 36 (2006) 555-608.
[58] M. Asgari, A. Barnoush, R. Johnsen, R. Hoel, Microstructural characterization of pulsed plasma nitrided 316L stainless steel, Mater. Sci. Eng. A 529 (2011) 425-434.
[59] R. Gibala, A.J. Kumnick, Hydrogen Embrittlement and Stress Corrosion Cracking Edited by R. Gibala and R. F. Hehemann (1984) 61-77.
[60] A. Griesche, E. Dabah, T. Kannengiesser, N. Kardjilov, A. Hilger, I. Manke, Three-dimensional imaging of hydrogen blister in iron with neutron tomography, Acta Mater. 78 (2014) 14-22.
[61] M.C. Tiegel, M.L. Martin, A.K. Lehmberg, M. Deutges, C. Borchers, R. Kirchheim, Crack and blister initiation and growth in purified iron due to hydrogen loading, Acta Mater. 115 (2016) 24-34.

[62] E.P. Georgiou, V.P. Cevallos, T. Van der Donck, D. Drees, J. Meersschaut, N. Panagopoulos, J.P. Celis, Effect of cathodic hydrogen charging on the wear behavior of 5754 Al alloy, Wear 390-391 (2017) 295-301.
[63] Y.V. Banakhevych, O.V. Hembara, O.E. Andreikiv, Numerical analysis of the kinetics of propagation of hydrogen blisters in the oil-and-gas equipment, Mater. Sci. 45(5) (2009) 626-637.
[64] B. Farahmand, Virtual testing and predictive modeling: for fatigue and fracture mechanics allowables, Springer, Boston, MA2009.
[65] C.S. Marchi, B.P. Somerday, S.L. Robinson, Permeability, solubility and diffusivity of hydrogen isotopes in stainless steels at high gas pressures, Int. J. Hydrog. Energy 32(1) (2007) 100-116.
[66] J. Venezuela, C. Tapia-Bastidas, Q.J. Zhou, T. Depover, K. Verbeken, E. Gray, Q.L. Liu, Q. Liu, M.X. Zhang, A. Atrens, Determination of the equivalent hydrogen fugacity during electrochemical charging of 3.5NiCrMoV steel, Corros. Sci. 132 (2018) 90-106.
[67] P.D. Hicks, Altstetter, C.J. , Comparison of internal hydrogen embrittlement of superalloys 718 and 625, JOM (1991) pp 635–651.
[68] A.E. Pontini, J.D. Hermida, X-ray diffraction measurement of the stacking fault energy reduction induced by hydrogen in an AISI 304 steel, Scr. Mater. 37(11) (1997) 1831-1837.
[69] S.B. Dai, W.C. Liu, First-principles study on the structural, mechanical and electronic properties of delta and gamma " phases in Inconel 718, Comp. Mater. Sci. 49(2) (2010) 414-418.
[70] M. Hoelzel, S.A. Danilkin, H. Ehrenberg, D.M. Toebbens, T.J. Udovic, H. Fuess, H. Wipf, Effects of high-pressure hydrogen charging on the structure of austenitic stainless steels, Mater. Sci. Eng. A 384(1-2) (2004) 255-261.
[71] R. Kirchheim, A. Pundt, 25 - Hydrogen in Metals, in: D.E. Laughlin, K. Hono (Eds.), Physical Metallurgy (Fifth Edition), Elsevier, Oxford, 2014, pp. 2597-2705.
[72] W. Abuzaid, H. Sehitoglu, Critical resolved shear stress for slip and twin nucleation in single crystalline FeNiCoCrMn high entropy alloy, Mater. Charact. 129 (2017) 288-299.
[73] T. Depover, E. Wallaert, K. Verbeken, On the synergy of diffusible hydrogen content and hydrogen diffusivity in the mechanical degradation of laboratory cast Fe-C alloys, Mater. Sci. Eng. A 664 (2016) 195-205.
[74] H. Luo, Z.M. Li, W.J. Lu, D. Ponge, D. Raabe, Hydrogen embrittlement of an interstitial equimolar high-entropy alloy, Corros. Sci. 136 (2018) 403-408.
[75] K.E. Nygren, S. Wang, K.M. Bertsch, H.B. Bei, A. Nagao, I.M. Robertson, Hydrogen embrittlement of the equi-molar FeNiCoCr alloy, Acta Mater. 157 (2018) 218-227.
[76] G.C. Obasi, Z. Zhang, D. Sampath, R. Morana, R. Akid, M. Preuss, Effect of microstructure and alloy chemistry on hydrogen embrittlement of precipitation-hardened Ni-based alloys, Metall. Mater. Trans. A 49a(4) (2018) 1167-1181.
[77] G. Odemer, E. Andrieu, C. Blanc, Influence of hydrogen on electrochemical behavior of Ni-based superalloy 718, Int. J. Hydrog. Energy 43(2) (2018) 1006-1011.
[78] I.M. Robertson, The effect of hydrogen on dislocation dynamics, Eng. Fract. Mech. 68(6) (2001) 671-692.
[79] P.J. Ferreira, I.M. Robertson, H.K. Birnbaum, Influence of hydrogen on the stacking-fault energy of an austenitic stainless steel, Mater. Sci. Forum 207-209 (1996) 93-96.

[80] J.D. Hermida, A. Roviglione, Stacking fault energy decrease in austenitic stainless steels induced by hydrogen pairs formation, Scr. Mater. 39(8) (1998) 1145-1149.
[81] W.A.T. Clark, R.H. Wagoner, Z.Y. Shen, T.C. Lee, I.M. Robertson, H.K. Birnbaum, On the Criteria for Slip Transmission across Interfaces in Polycrystals, Scr. Metall. Mater. 26(2) (1992) 203-206.
[82] N. Kheradmand, A.F. Knorr, M. Marx, Y. Deng, Microscopic incompatibility controlling plastic deformation of bicrystals, Acta Mater. 106 (2016) 219-228.
[83] T.C. Lee, I.M. Robertson, H.K. Birnbaum, TEM in situ deformation study of the interaction of lattice dislocations with grain boundaries in metals, Philos. Mag. A 62(1) (1990) 131-153.
[84] E.A. West, G.S. Was, A model for the normal stress dependence of intergranular cracking of irradiated 316L stainless steel in supercritical water, J. Nucl. Mater. 408(2) (2011) 142-152.
[85] T.C. Lee, I.M. Robertson, H.K. Birnbaum, Prediction of Slip Transfer Mechanisms across Grain-Boundaries, Scr. Metall. Mater. 23(5) (1989) 799-803.
[86] E. Werner, W. Prantl, Slip transfer across grain and phase boundaries, Acta Metall. Mater. 38(3) (1990) 533-537.
[87] I. Adlakha, K.N. Solanki, Critical assessment of hydrogen effects on the slip transmission across grain boundaries in alpha-Fe, Proc. Math. Phys. Eng. Sci. 472(2185) (2016).
[88] R. Kirchheim, Reducing grain boundary, dislocation line and vacancy formation energies by solute segregation. I. Theoretical background, Acta Mater. 55(15) (2007) 5129-5138.

Figure(s)

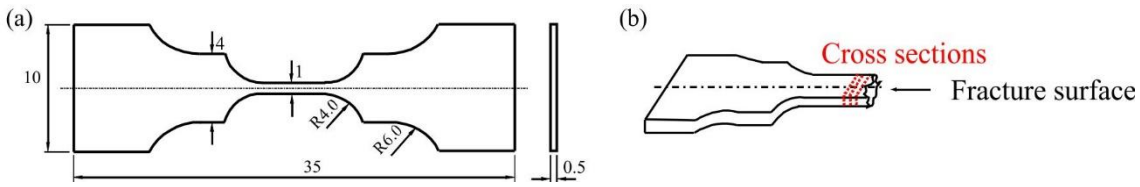

Fig. 1 (a) Specimen geometry for slow strain rate tensile test (all dimensions are shown in mm) and (b) schematic of subsurface characterization direction.

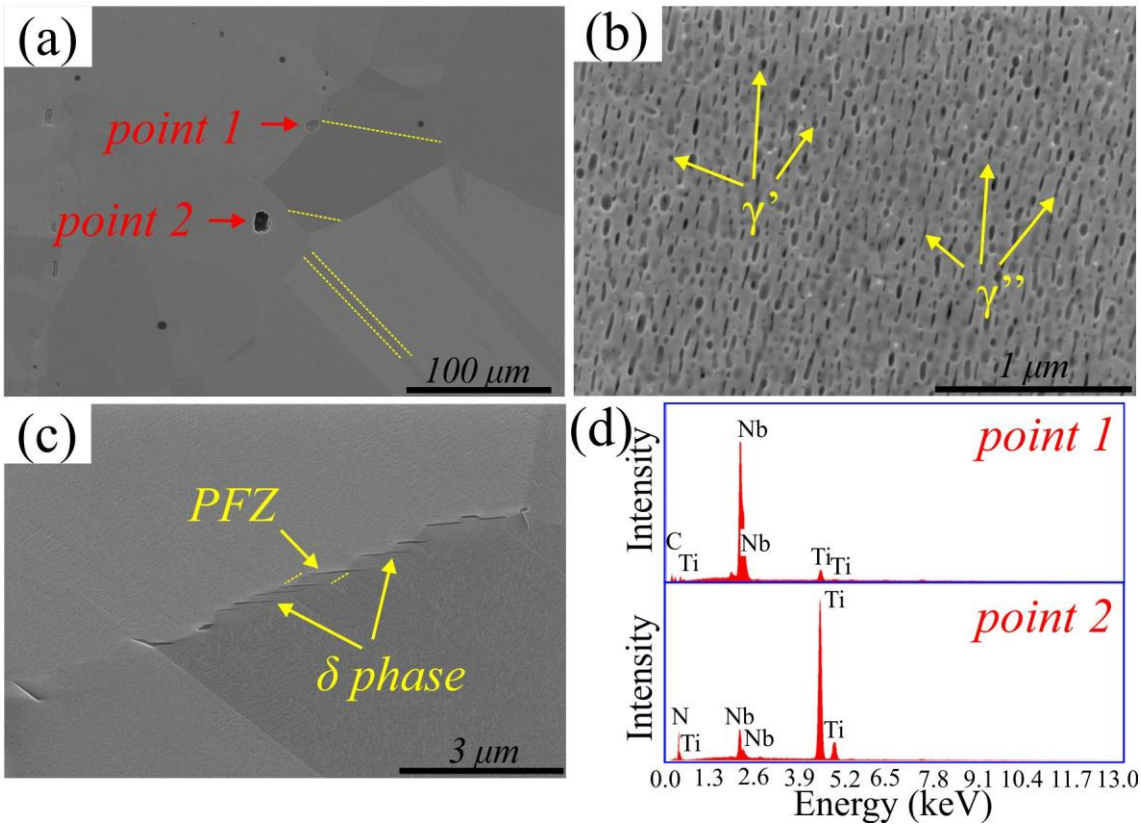

Fig. 2 Microstructure of Alloy 718 showing (a) carbides, (b) fine γ' and γ'' precipitates, and (c) the δ phase. (d) EDS information on incoherent (Nb, Ti)N nitrides and (Nb, Ti)C carbides.

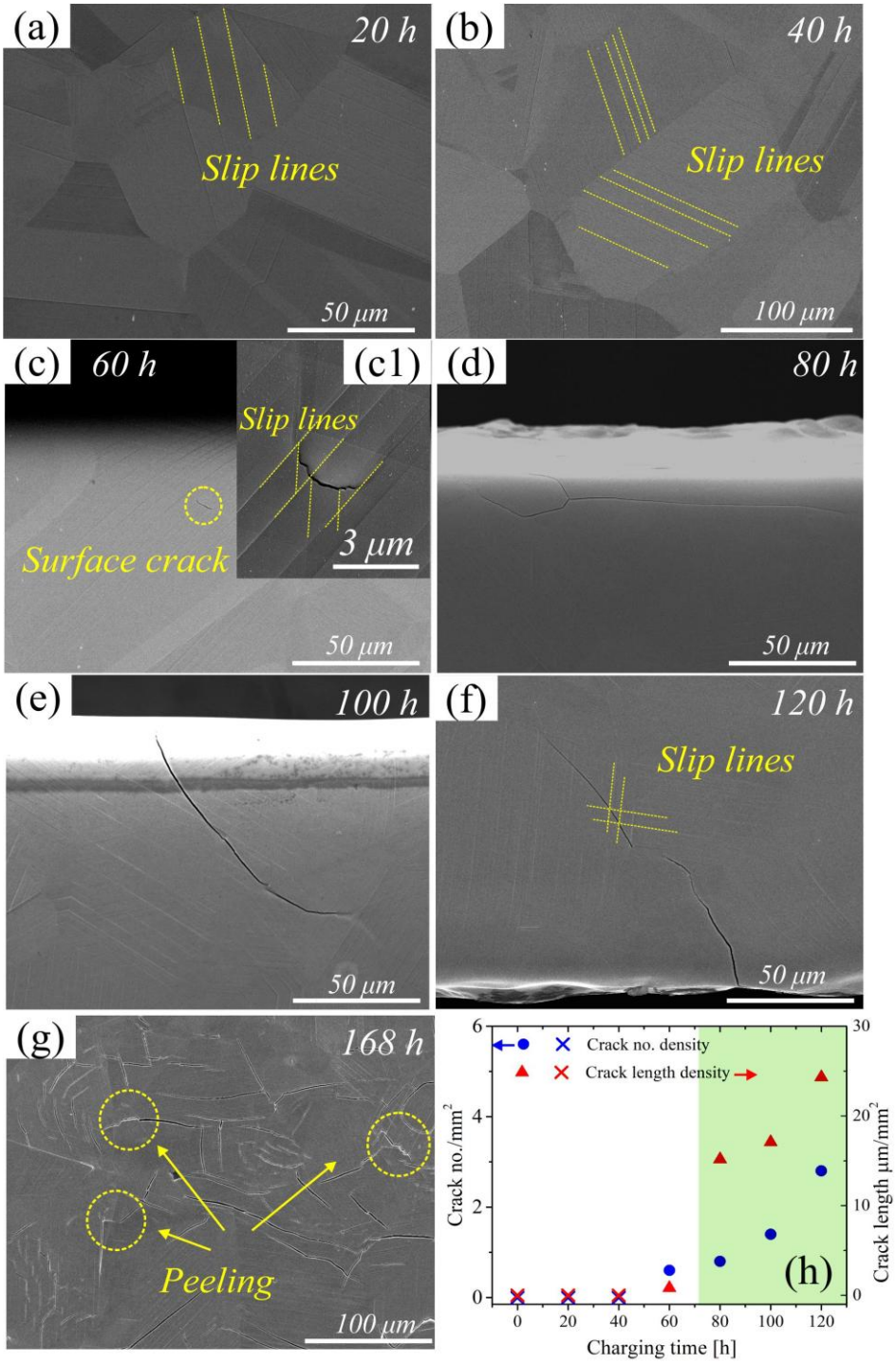

Fig. 3 BSE images ((a)-(c)), and SE images ((d)-(g)) showing slip lines and surface cracks on Alloy 718 samples after electrochemical charging. The magnified view of the area

highlighted by dashed circle in (c) is shown in (c1). (h) Statistical summary of the crack number and crack length densities on the surfaces after charging from 20 h to 120 h.

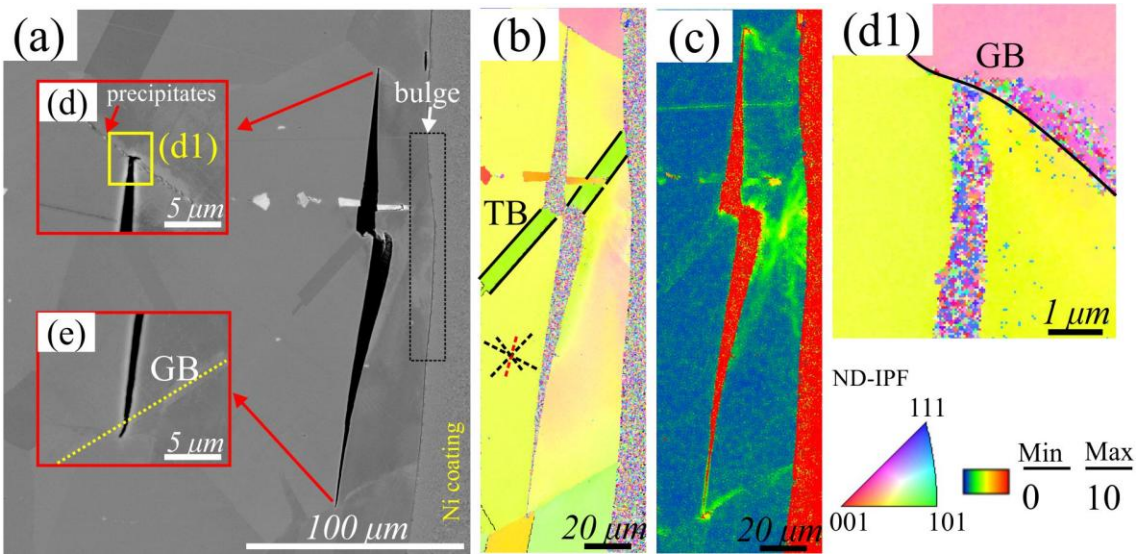

Fig. 4 SEM and EBSD analysis of subsurface cracks in the 120 h charged sample. (a), (d), and (e) Micrographs illustrating crack paths. (b) ND-IPF (inverse pole figure) map and (c) KAM map of the crack. (d1) is the ND-IPF map of the area highlighted by the yellow box in (d). (TB: twin boundary, GB: grain boundary. The color scale of the IPF maps is shown in the IPF triangle. The color scale of the KAM map is shown in the color bar.)

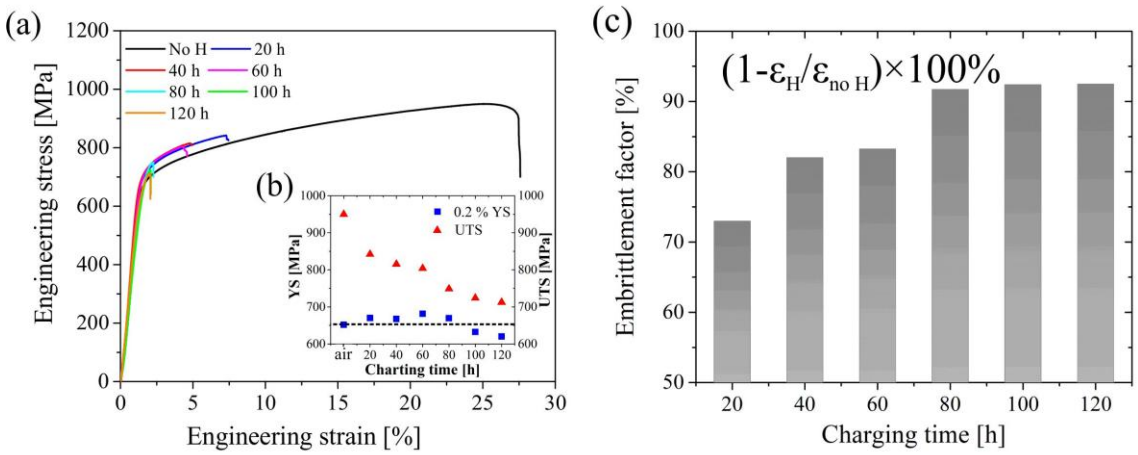

Fig. 5 (a) Engineering stress-strain curves of the tested specimens under different charging conditions. Effect of hydrogen on (b) 0.2 % YS and UTS (b) and (c) EF.

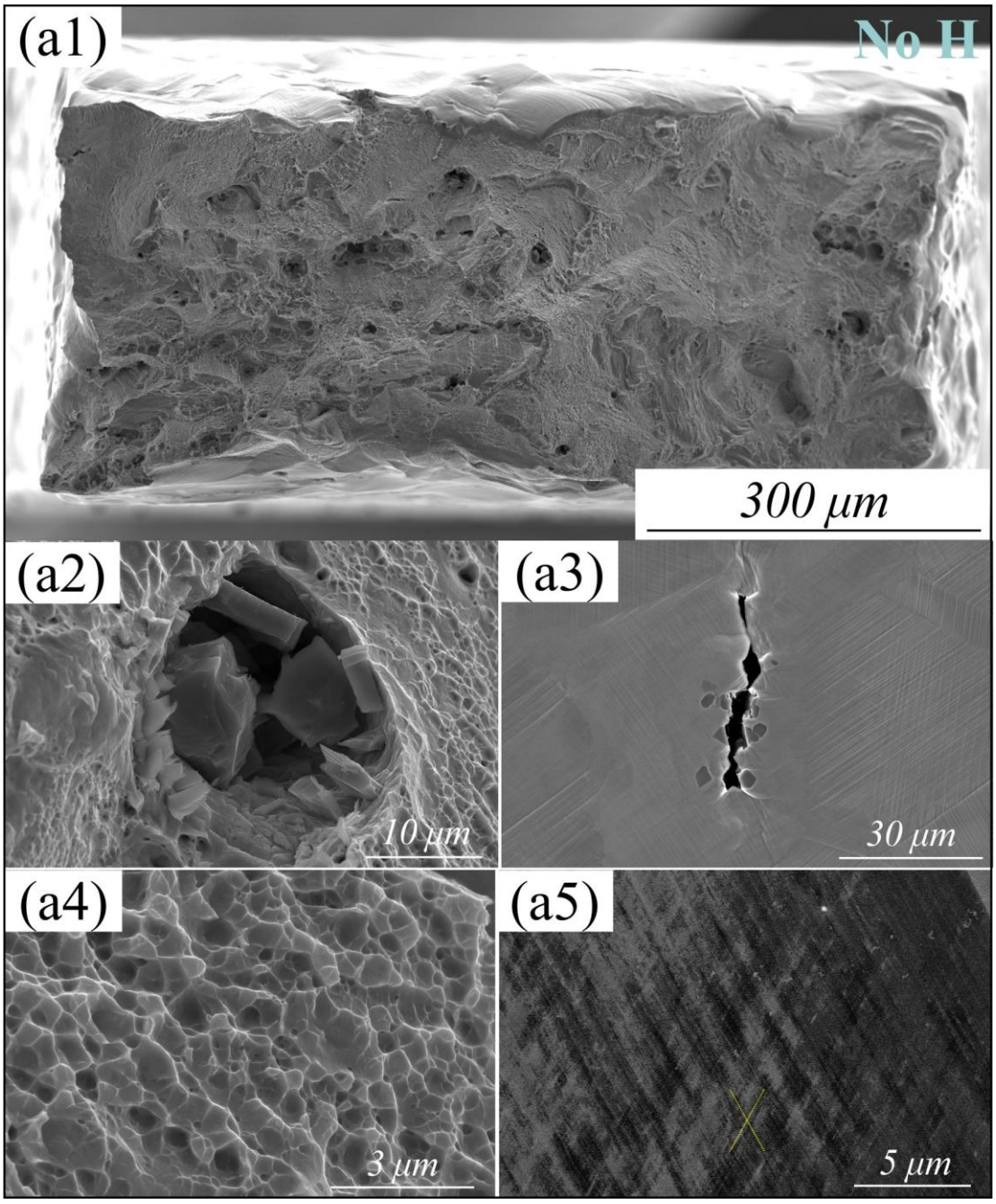
(a1)
No H
300 μm
(a2)
10 μm
(a3)
30 μm
(a4)
3 μm
(a5)
5 μm

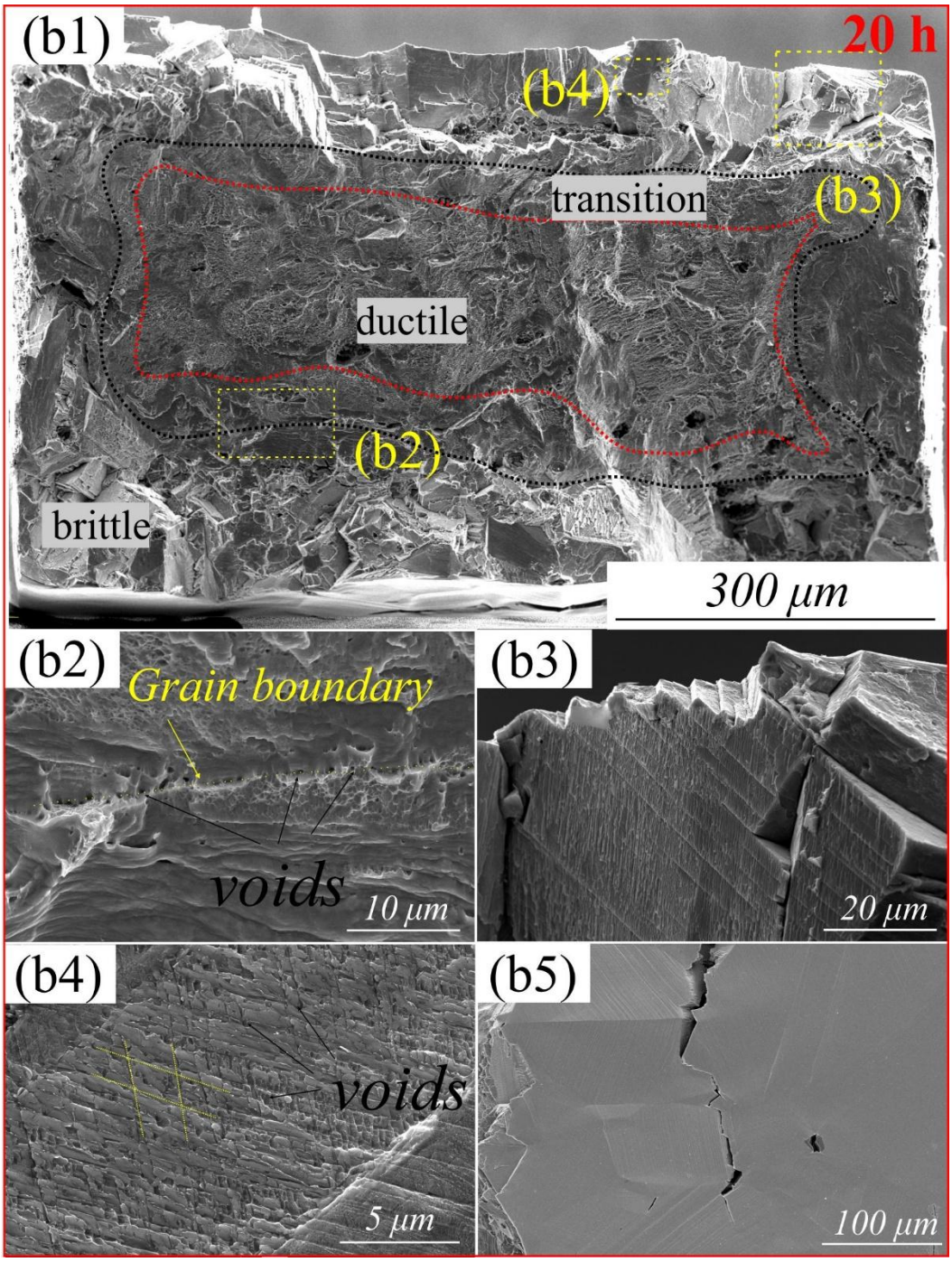

Fig. 6 (a1)-(a5): Micrograph analysis of no-hydrogen sample after failure showing (a1, a4) ductile fracture features, (a2, a3) carbonitride cracks, and (a5) surface slip lines; (b1)-(b5): micrograph analysis of a fractured sample with 20 h-charging showing (b1) transition from brittle to ductile fracture, (b2) GB microvoids, (b3) transgranular steps, (b4) microvoids at slip lines intersections, and (b5) surface secondary cracks.

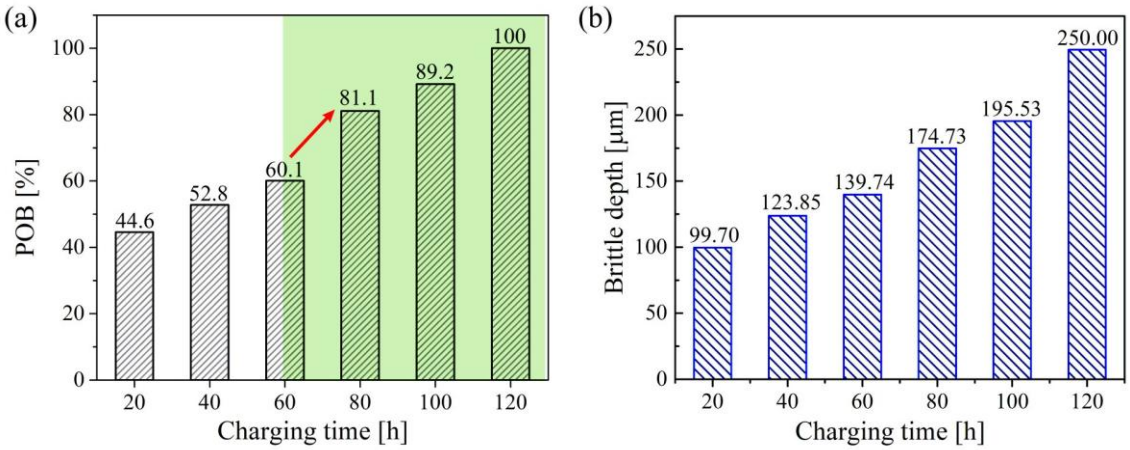

Fig. 7 Effect of hydrogen on (a) POB and (b) the corresponding brittle depth.

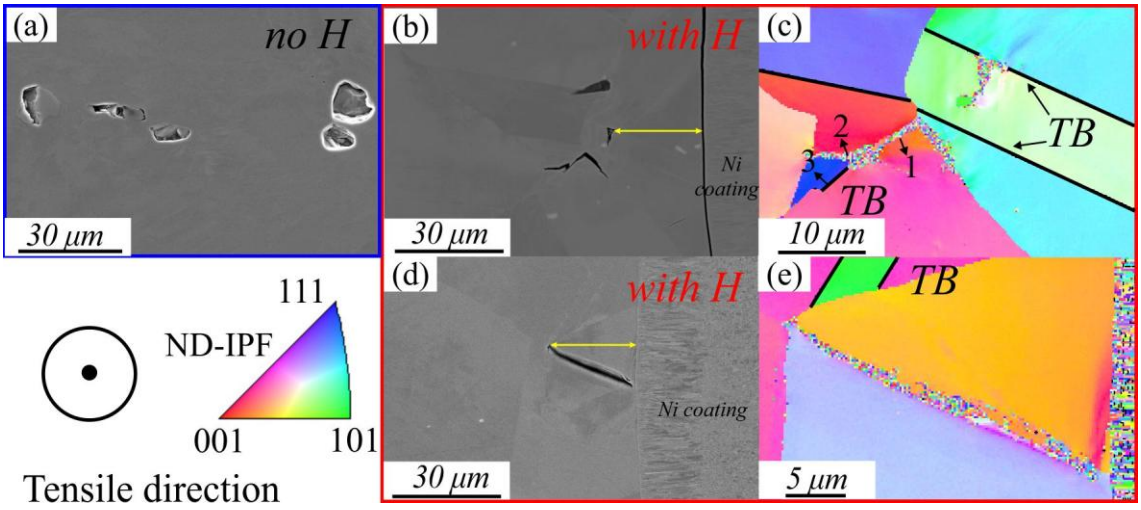

Fig. 8 Micrographs of the cross sections of (a) a hydrogen-free sample showing carbides cracks. (b)-(c) BSE images and ND-IPF maps, respectively, of a hydrogen-charged sample showing both intergranular and transgranular cracks. (d)-(e) BSE images and ND-IPF maps, respectively, of a hydrogen-charged sample showing only intergranular cracks, step size: 0.2 μm.

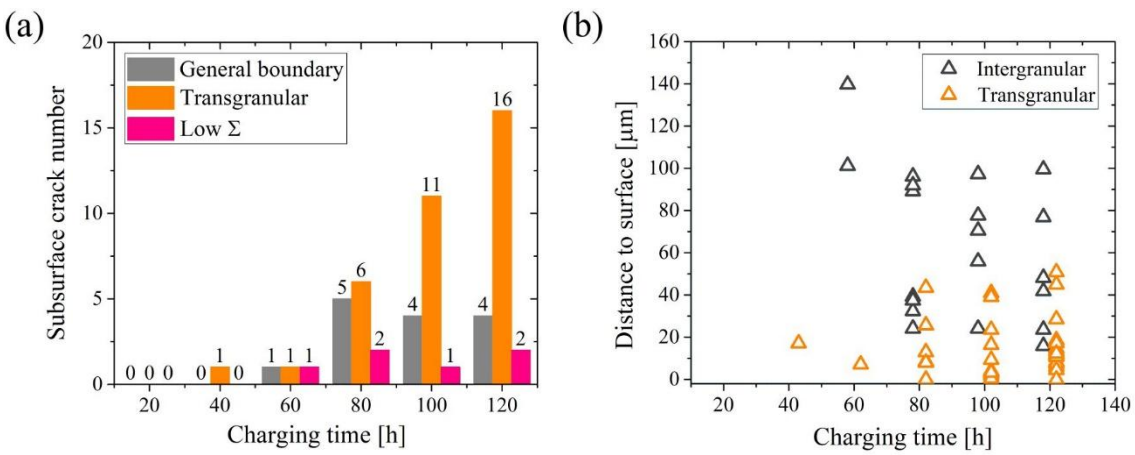

Fig. 9 Statistical analysis of subsurface cracks: (a) the number of different types of cracks on the gauge area ($5mm^2$) and (b) distance between surface and cracks.

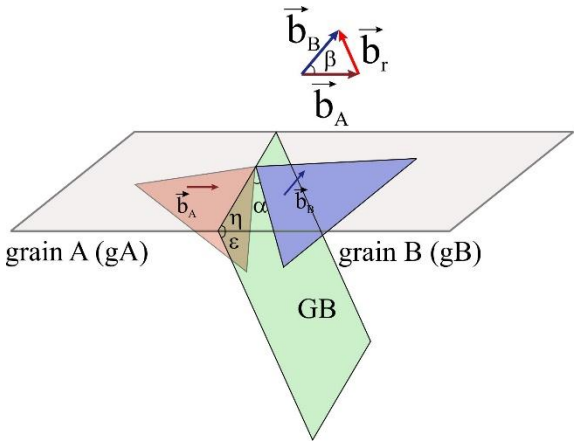

Fig. 10 Schematic of slip system coupling at a GB, together with GB traces, represented by angles (η, ε).

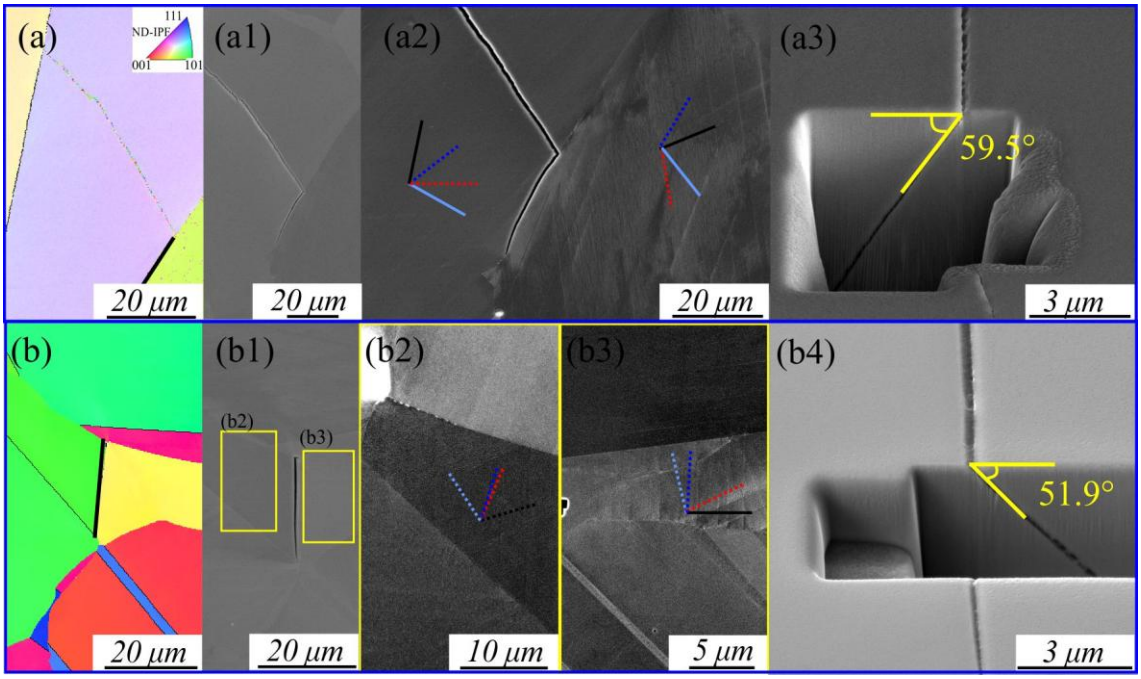

Fig. 11 ND-IPF maps (a) (b), and corresponding SE images (a1) and (b1) showing GB cracks. The ECC micrographs (a2) (b2)-(b3) indicate active slip lines that represent {111} traces (the magnitude of Schmid factors varies from the highest to the lowest value: red, blue, light blue, black; the active slip planes are marked in dotted lines), (b2)-(b3) are magnified ECC images of areas in (b1) that are marked in yellow. (a3) (b4) The FIB cross sections show GB depth tilt angles.

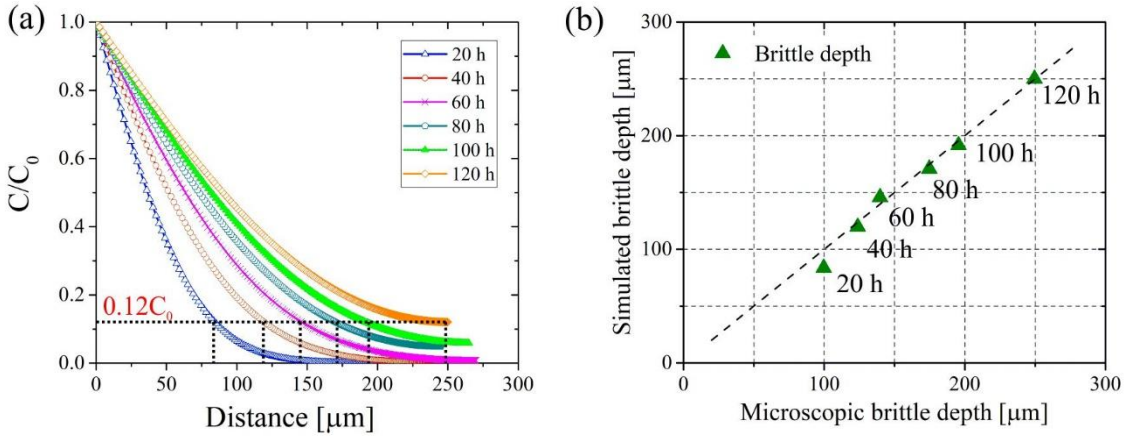

Fig. 12 (a) Hydrogen concentration profile for different charging time and (b) comparison of hydrogen effect on brittle depth measured from fracture surface and the simulated 0.12 C_0 results.

Table(s)

Table 1 Chemical composition of the tested Alloy 718.

Element	C	Fe	Cr	Nb	Mo	Ti	Al	Co	Ni
wt. %	0.018	19.14	17.62	4.98	2.87	0.95	0.52	0.05	Balance

Table 2 Measured GB parameters, active slip planes with corresponding SFs, and GB resistance calculated from eq. (3). (U V W)/ θ represents the misorientation axis and angle between adjacent grains.

C-GB	Euler angle (φ1 Φ φ2)	GB parameter (U V W)/θ	η, ε	Active slip plane (hkl)	SF	α (≤ 15°) $(h_ak_al_a)$–$(h_bk_bl_b)$	Min. ω $(h_ak_al_a)$–$(h_bk_bl_b)$
gA1	(12.1 60.7 287.2)	(-5 0 -1) /55.4	63.3, 59.5	(-1-11) (-111)	0.48 0.39	no	0.83 (-1-11)–(-111)
gB1	(250.4 151.6 353.6)			(111) (-111)	0.48 0.47		
gA2	(194.8 27.9 33.1)	(1 -1 -1) /49.3	26.6, 90.0	(-111) (1-11) (111)	0.47 0.40 0.39	no	0.23 (1-11)–(1-11)
gB2	(98.4 46.5 340)			(1-11) (-1-11)	0.46 0.40		
gA3	(308.9 24.5 98.6)	(-1 1 -1) /29.9	51.9 51.9	(111) (1-11) (-1-11)	0.49 0.48 0.31	14.4 (111)–(1-11)	0.14 (1-11)–(1-11)
gB3	(249.9 90.1 317.7)			(1-11) (-111) (111) (-1-11)	0.43 0.42 0.05 0.02	5.5 (1-11)–(1-11)	

NC-GB	Euler angle (φ1 Φ φ2)	GB parameter (U V W)/θ	η, ε	Active slip plane	SF	α (≤ 15°) $(h_ak_al_a)$–$(h_bk_bl_b)$	Min. ω $(h_ak_al_a)$–$(h_bk_bl_b)$
gA4	(12.1 60.7 287.2)	(-7 -1 0) /46.8	64.0, 88.8	(-1-11) (-111)	0.48 0.39	11.5 (-1-11)–(111)	0.09 (-1-11)–(111)
gB4	(59.4 158.5 266.0)			(111) (1-11)	0.49 0.49		
gA5	(225.6 87.2 302.0)	(7 1 0) /16.4	13.2, 89.0	(1-11) (-111)	0.48 0.47	1.1 (-111)–(-111)	0.01 (-111)–(-111)
gB5	(239.0 77.8 297.8)			(1-11) (-111) (-1-11)	0.49 0.42 0.33	12.2 (1-11)–(-1-11)	
gA6	(12.1 60.7 287.2)	(-1 1 -1) /51.9	26.3, 76.4	(-1-11) (-111)	0.48 0.39	1.3 (-111)–(1-11)	0.04 (-111)–(1-11)
gB6	(239.0 77.8 297.8)			(1-11) (-111) (-1-11)	0.49 0.42 0.33	12.8 (-111)–(-1-11)	

gA7	(308.9 24.5 98.6)	(0 -1 -1) /34.8	82.6, 44.2	(111) (1-11) (-1-11)	0.49 0.48 0.31	1.8 (111)– (-1-11)	0.1 (-1-11)– (-111)
gB7	(76.8 82.1 3.8)			(-111) (111) (-1-11)	0.46 0.45 0.42	3.3 (-1-11)– (-111)	
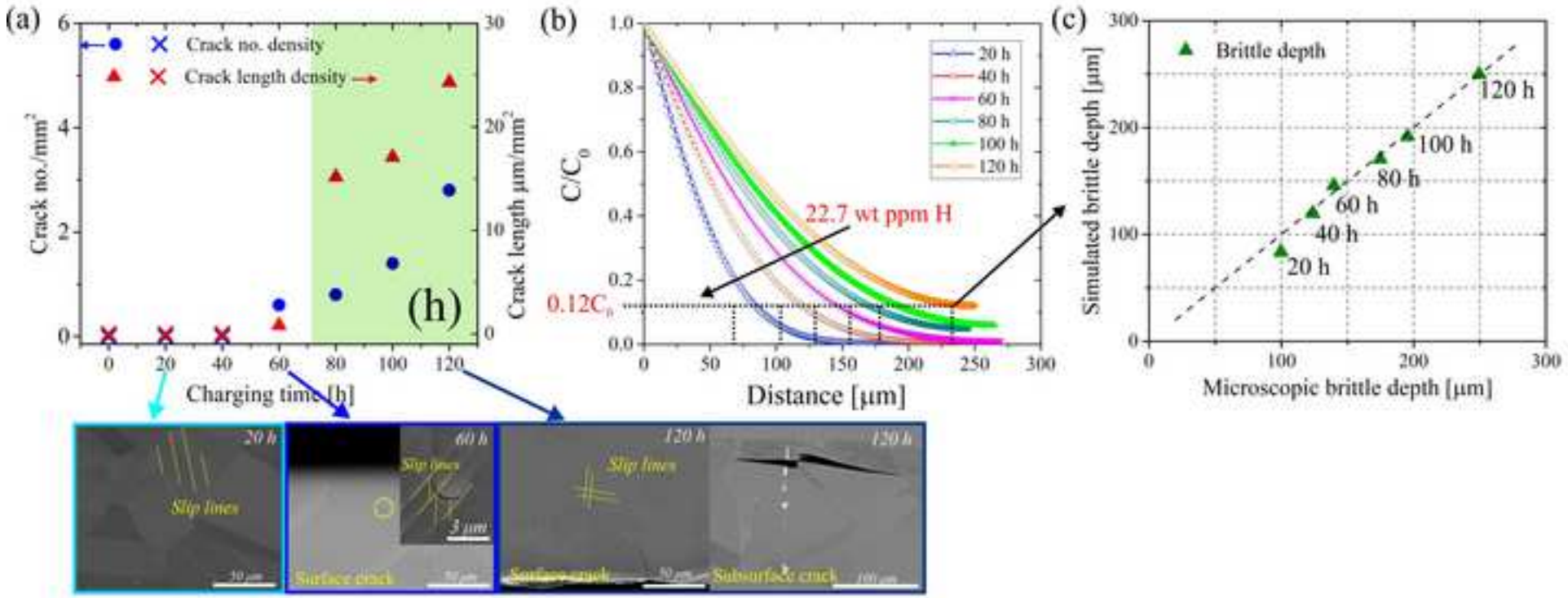
*Graphical Abstract